

Improving the numerical modelling of droplet breakup for spray flows

C. Sula · H. Grosshans ·
M.V. Papalexandris

Received: date / Accepted: date

Abstract In this paper we examine droplet behavior and macroscopic atomization characteristics of a non-reactive liquid spray via a series of Large-Eddy Simulations. In our numerical study we examine three popular models for spray atomization, namely, the Taylor Analogy Breakup (TAB), Reitz-Diwakar and Pilch-Erdman models, and compare their predictions against available experimental data. According to our simulations, and for the flow conditions considered herein, the TAB model exhibits a slightly better performance than the other two models do. Further, since the TAB model is known to underestimate the effect of disruptive drag forces, we present a modification to it and assess its predictive capacity. More specifically, we show that our modification leads to improved accuracy in the numerical computation of important global quantities of the spray, such as the liquid-penetration and the vapor-penetration distance.

Keywords spray · atomization · secondary breakup · droplets · Large-Eddy Simulations

C. Sula
Institute of Mechanics, Materials and Civil Engineering,
Université catholique de Louvain, 1348 Louvain-la-Neuve, Belgium
E-mail: constantin.sula@uclouvain.be

H. Grosshans
Physikalisch-Technische Bundesanstalt (PTB),
Bundesallee 100, 38116 Braunschweig, Germany
E-mail: holger.grosshans@ptb.de

M.V. Papalexandris
Institute of Mechanics, Materials and Civil Engineering,
Université catholique de Louvain, 1348 Louvain-la-Neuve, Belgium
E-mail: miltiadis.papalexandris@uclouvain.be

1 Introduction

Research on sprays has received a lot of attention due to their applications in diverse technological areas such as materials processing, manufacturing technologies, internal combustion engines, to name but a few. However, the processes occurring in spray flows, such as droplet breakup and evaporation, are quite complex and are characterized by a multitude of spatial and temporal scales. For this reason, the study of sprays, either experimentally or numerically, entails significant challenges. Modern computer technology has made possible the simulation of spray flows; this, however, still relies on numerical modelling of droplet breakup.

Earlier experimental studies of injection of high-pressure liquid into a quiescent gas [38,17,46] focused on the understanding of the fundamental mechanisms underpinning jet atomization, namely, the primary and secondary breakups. The primary breakup is the disintegration of the core of the liquid jet. The secondary breakup also referred to as ‘‘droplet breakup’’ herein, is the splitting of the droplets generated by the primary breakup into smaller ones. This process is accompanied by phenomena such as interphasial heat transfer and droplet evaporation that must also be accounted for.

Also, previous investigations have confirmed the dependency of the secondary breakup on the physical properties of the liquid and surrounding gas, such as viscosities, mass densities and liquid surface tension. For example, Elktob [11] showed that high liquid viscosity leads to larger droplet sizes, poor atomization and, therefore, longer liquid penetration distances. Surface tension affects the droplet size since it opposes the distortion of the droplet surface. Moreover, according to Elktob [11], liquid density also plays an important role because it is linked to the kinetic energy of the droplets, which is one of the primary factors that determine spray behavior. Further, Faeth et al. [12] reported a strong correlation between atomization, mixing conditions and geometry of the nozzle.

The combined influence of these parameters can be encapsulated in two nondimensional groups, namely, the Weber number $We = \rho \mathbf{u}_{\text{rel}}^2 r_d / \sigma$ and the Ohnesorge number $Oh = \mu_d / (\rho_d d_d \mathbf{u}_{\text{rel}})^{0.5}$, where ρ is the gas density, \mathbf{u}_{rel} is the relative velocity between the droplet and the gas, r_d and d_d are the droplet radius and diameter, while μ_d and σ are the liquid viscosity and surface tension respectively. Based on the magnitude of We , different breakup regimes are distinguished which have been referred to as vibrational breakup, bag breakup, bag/streamer breakup, stripping breakup and catastrophic breakup [45].

Over the years, many numerical models for droplet breakup have been developed. Popular examples are the Taylor Analogy Breakup (TAB) model of O’Rourke and Amsden [30], the Reitz-Diwakar (RD) model [39], the Pilch-Erdman (PE) model [34], and the model of Ibrahim et al. [18], to name but a few. These models are intended to be applied to Eulerian-Lagrangian simulations, according to which the spray droplets are treated in a Lagrangian framework. In addition to those Eulerian-Lagrangian approaches, models for

Eulerian-Eulerian simulations have also been developed; see, for example, [21, 25, 47] and references therein.

In the past, various researchers used such models in spray-flow simulations and assessed their performance via comparisons with experimental measurements; see, for example, [15, 29] and references therein. An examination of the literature shows that none of the available models can predict all the facets of droplet breakup with good accuracy. The main reason for this is that the various models necessarily invoke several simplifying assumptions and contain parameters whose values are problem-dependent, thereby reducing their ranges of applicability.

Amongst the afore-mentioned models, the TAB model is perhaps the most grounded on the physical mechanisms that occur during droplet breakup. Over the years, various researchers have tried to address its shortcomings and presented upgraded versions of it. For example, the results of Beatrice et al. [3] showed that it has the tendency to underpredict the droplet lifetime which, in turn, diminishes its accuracy when applied to high-pressure sprays. To remedy this, Bianchi and Pelloni [4] tuned the model constants so that the computed droplet lifetime matched the experimental correlation of Pilch and Erdman [34].

Despite these improvements, discrepancies remained between experimental data and numerical prediction for other quantities, such as liquid penetration distance. Also, in order to better match the experimental data for liquid penetration, Tanner [42] proposed to consider deformed droplets so as to prolong their lifetime. Similarly, Park et al. [31] introduced a more physically substantiated breakup criterion which has the potential to better predict droplet lifetime. It is also worth mentioning that according to Matysiak [26], the TAB model can underestimate the effect of the disruptive drag forces.

In the present study we first perform simulations of secondary breakup and evaporation of a liquid spray using the aforementioned TAB, RD and PE models, and quantify the differences between them via comparisons with experimental data. Subsequently, motivated by the discussion in [26], we propose a new modification to the original TAB model so as to better capture the effect of the drag forces. The proposed modified TAB model will be referred to herein as MTAB. The improved capability of the MTAB model to predict both liquid and vapor penetration distances is evidenced via comparisons with experimental data which are also included herein.

Our study is based on Large-Eddy Simulations (LES) of the flow of interest. To this end, we employ a coupled Eulerian-Lagrangian formulation for the representation of the spray dynamics and the interaction between the two phases. In other words, we employ an Eulerian approach for the gaseous phase and Lagrangian particle tracking for the liquid droplets assuming two-way coupling between the gaseous phase and the droplets. Our target application is the flow that occurs when liquid fuel is injected into a Diesel engine. For this purpose, the numerical setup is based on the Engine Combustion Network “Spray A” [10] operating conditions. Accordingly, n-dodecane is chosen as the liquid fuel.

The paper is structured as follows. In Section 2 we present the governing equations for the ambient gas and the mathematical model for the dispersed liquid phase. In Section 3, we outline the three secondary breakup models that we use in our numerical study. Then, on Section 4 we describe the proposed modification to the original TAB model. In Section 5 we present the details of the numerical setup and analyze our numerical results, including comparisons against experimental data. We also elaborate on the probability distribution functions for the far-field droplet size and how this is affected by the breakup models. Finally, Section 6 concludes.

2 Governing Equations

The Large-Eddy Simulations (LES) of our study are based on the spatially-filtered, compressible Navier-Stokes-Fourier equations. Additionally, we employ the density-weighted operator of Favre [13]. Applied to a generic quantity ϕ , the corresponding Favre-filtered quantity $\tilde{\phi}$ is defined as $\tilde{\phi} = \overline{\rho\phi}/\bar{\rho}$, where $\bar{\rho}$ and $\overline{\rho\phi}$ are spatially-filtered quantities. In order to keep the notation simple, all the quantities associated to the ambient gas will appear without subscript; for example, the gas density will be denoted by ρ . On the other hand, all quantities associated to the droplets will have a descriptive subscript; for example, the droplet density will be denoted by ρ_d .

Upon Favre-filtering, the governing equations describing the balance of mass, momentum, energy and species of the continuous phase (i.e. the carrier gas), read:

$$\frac{\partial \bar{\rho}}{\partial t} + \nabla \cdot (\bar{\rho} \tilde{\mathbf{u}}) = \bar{I}, \quad (1)$$

$$\frac{\partial (\bar{\rho} \tilde{\mathbf{u}})}{\partial t} + \nabla \cdot (\bar{\rho} \tilde{\mathbf{u}} \tilde{\mathbf{u}}) = -\nabla \bar{p} + \nabla \cdot \left((\bar{\mu} + \mu_t) \tilde{\mathbf{V}}^d \right) + \bar{\mathbf{F}}, \quad (2)$$

$$\begin{aligned} \frac{\partial (\bar{\rho} \tilde{E})}{\partial t} + \nabla \cdot (\bar{\rho} \tilde{E} \tilde{\mathbf{u}}) &= -\nabla \cdot (\bar{p} \tilde{\mathbf{u}}) + \nabla \cdot \left((\bar{\mu} + \mu_t) \tilde{\mathbf{V}}^d \cdot \tilde{\mathbf{u}} \right) \\ &+ \nabla \cdot \left((\bar{\kappa} + \kappa_t) \nabla \tilde{T} \right) + \bar{Q}, \end{aligned} \quad (3)$$

$$\frac{\partial (\bar{\rho} \tilde{Y}_i)}{\partial t} + \nabla \cdot (\bar{\rho} \tilde{Y}_i \tilde{\mathbf{u}}) = \nabla \cdot \left(\bar{\rho} (\bar{D}_i + D_{it}) \nabla \tilde{Y}_i \right) + \bar{\Omega}_i, \quad i = 1, \dots, N-1, \quad (4)$$

where the N is the number of gaseous species. In our study, the gaseous phase initially consists of nitrogen, carbon dioxide and water vapor. Therefore, the gaseous species are N_2 , CO_2 , H_2O , fuel vapor (fv), ie $N = 4$.

Following standard notation, $\bar{\rho}$, \bar{p} , \tilde{E} and $\tilde{\mathbf{u}} = (\tilde{u}, \tilde{v}, \tilde{w})$ denote, respectively the filtered fluid density, pressure, total energy and velocity vector. Also, \tilde{Y}_i represents the filtered mass fraction of the i -th gaseous species, where $i =$

CO₂, H₂O and fv. Additionally, in the above equation $\tilde{\mathbf{V}}^d$ stands for twice the deviatoric part of the filtered strain-rate tensor, $\tilde{\mathbf{V}} = \frac{1}{2} (\nabla \tilde{\mathbf{u}} + (\nabla \tilde{\mathbf{u}})^\top)$.

Further, $\bar{\mu}$, $\bar{\kappa}$ and \bar{D}_i represent, respectively, the filtered viscosity, thermal conductivity and species diffusivities of the carrier gas. Herein, for each species we assume binary diffusion with respect to the dominant constituent N₂.

In the governing system (1)-(4) the source terms \bar{T} , \bar{F} , \bar{Q} and $\bar{\Omega}_i$ describe the interactions between the continuous gaseous phase and the dispersed liquid one. More specifically, \bar{T} accounts for phase change, i.e. the evaporation of the liquid fuel. Also, $\bar{\Omega}_i$ accounts for the source terms in the concentration of the gaseous species due to evaporation. Due to the fact that no chemical reaction occurs between the gaseous species, the overall masses of N₂, CO₂ and H₂O remain constant. Therefore, only $\bar{\Omega}_{fv}$ is non-zero, so that the following relation holds,

$$\bar{\Omega}_{fv} = \bar{T}. \quad (5)$$

Further, the integral of \bar{T} over a control volume is equal to the evaporation rate of the droplets inside the control volume. For example, if the control volume is a computational cell, then the following relation holds,

$$\int_{V_{\text{cell}}} \bar{T} dV = \sum_{i=1}^{N_{\text{cell}}} \dot{m}_{d,i}. \quad (6)$$

In this equation V_{cell} stands for the volume of the computational cell, N_{cell} stands for the number of particles inside V_{cell} . Further, $\dot{m}_{d,i}$ denotes the evaporation rate of the i -th droplet and its expression is given by (20) below.

The source term \bar{F} accounts for the momentum transfer between the fuel droplets and the surrounding gas. Its integral over a computational cell is equal to the opposite of the sum of the aerodynamic drag forces acting on the droplets inside the cell,

$$\int_{V_{\text{cell}}} \bar{F} dV = \sum_i^{N_{\text{cell}}} \mathbf{f}_{d,i}, \quad (7)$$

where $\mathbf{f}_{d,i}$ is the aerodynamic drag experienced by the i -th droplet inside the computational cell and its expression is given by (15) below.

Further, the source term \bar{Q} represents the energy transfer between the liquid fuel droplets and the carrier gas. Its integral over a computational cell is equal to the opposite of the energy that the droplets inside the cell exchange with the carrier gas. For any given droplet, this energy exchange consists of three contributions: heat transfer, latent heat of evaporation and the work of the aerodynamic drag. Therefore, the following relation holds,

$$\int_{V_{\text{cell}}} \bar{Q} dV = \sum_{i=1}^{N_{\text{cell}}} (Q_{d,i} + \dot{m}_{d,i} h_{l,i} + \mathbf{f}_{d,i} \cdot \mathbf{u}_{d,i}), \quad (8)$$

where $Q_{d,i}$ is the heat-transfer rate between the i -th droplet and the surrounding gas, $h_{l,i}$ is the latent heat of evaporation of fuel at the temperature of the i -th droplet, and $\mathbf{u}_{d,i}$ is the velocity of the i -th droplet.

Finally, the system of equations is closed by the filtered thermal equation of state,

$$\bar{p} = \bar{\rho} \widetilde{RT}. \quad (9)$$

With respect to the subgrid-scale (SGS) modelling, the eddy viscosity μ_t is computed via the dynamic k -equation model [7, 49], while the thermal diffusivity κ_t is computed via μ_t by assuming a constant turbulent Prandtl number, namely, $Pr_t = 1$. The approach to compute the eddy viscosity is similar to that of the variable-density dynamic Smagorinsky model [27]. However, in this case, the reference velocity is taken to be square root of the SGS kinetic energy \sqrt{k} instead of $\Delta|\widetilde{\mathbf{V}}|$, with Δ being the nominal filter width. Accordingly, the eddy viscosity satisfies $\mu_t = C_s \Delta \bar{\rho} \sqrt{k}$, where C_s is a model coefficient that is computed dynamically from the Germano identity [27]. Moreover, the SGS kinetic energy is computed via the k -equation which reads,

$$\begin{aligned} \frac{\partial(\bar{\rho}k)}{\partial t} = & -\nabla \cdot (\bar{\rho}k\tilde{\mathbf{u}}) - \mu_t \widetilde{\mathbf{V}}^d \cdot \widetilde{\mathbf{V}} - \epsilon_s - \epsilon_c - \nabla \cdot \mathbf{f} + II \\ & + \nabla \cdot \left[\mu_t \widetilde{\mathbf{V}}^d \cdot \tilde{\mathbf{u}} + \bar{\mu} \nabla k + \bar{\mu} \nabla \cdot \left(\frac{\mu_t \widetilde{\mathbf{V}}^d}{\bar{\rho}} \right) + R \frac{\mu_t}{Pr_t} \nabla \widetilde{T} \right]. \end{aligned} \quad (10)$$

The closure of this equation requires models for \mathbf{f} , ϵ_s , ϵ_c and II . According to [7] the following models are proposed for these terms,

$$f = C_f \bar{\rho} \Delta \sqrt{k} \nabla k, \quad (11)$$

$$\epsilon_s = C_{\epsilon_s} \bar{\rho} k^{3/2} \Delta^{-1}, \quad (12)$$

$$\epsilon_c = C_{\epsilon_c} M_t^2 \bar{\rho} k^{3/2} \Delta^{-1}, \quad (13)$$

$$II = C_{II} \Delta^2 \nabla \bar{p} \nabla (\nabla \cdot \tilde{\mathbf{u}}). \quad (14)$$

In the above equations, C_f , C_{ϵ_s} , C_{ϵ_c} and C_{II} are closure coefficients that have to be determined empirically; for a detailed description on their calculation, the reader is referred to [7]. Also, the quantity M_t that appears in (13) is the SGS turbulent Mach number, $M_t = \sqrt{2k}/a$ with a being the mean speed of sound.

The governing equations (1)-(4) are discretized via a finite-volume approach and integrated in time via the implicit Euler scheme. With regard to spatial discretization, we employ the second-order upwind scheme for the convective terms and second-order centered differences for the diffusive terms. Also, for the numerical treatment of the momentum equation, we employ the PISO algorithm (Pressure-Implicit with Splitting of Operators) which is a popular method for the calculation of the pressure and velocity vector, originally proposed by Issa [20]. The simulations have been performed within the framework of the compressible LES solver ‘‘SprayFoam’’ of the open-source

software OpenFOAM[®] [44]. OpenFoam has been used extensively for simulations of particle-laden flows with two-way coupling. Recent numerical studies [14,37] have shown its reliability for this type of flows.

The motion of the droplets is computed numerically by combining Lagrangian Particle Tracking (LPT) and the stochastic parcel method [8]. According to this procedure, the droplets are grouped into parcels. It is also assumed that all droplets in a given parcel share the same properties, i.e. diameter d , velocity \mathbf{u}_d , density ρ_d , temperature T_d , etc.

For numerical purposes, each parcel is treated as a Lagrangian point and is tracked individually. With regard to droplet dynamics, we assume that the aerodynamic drag is the only force acting on the liquid-fuel droplets. Thus, the equation of motion reads,

$$\rho_d \frac{d\mathbf{u}_d}{dt} = \mathbf{f}_d = -\frac{3}{4} \frac{\rho}{d_d} C_D |\mathbf{u}_{\text{rel}}| \mathbf{u}_{\text{rel}}. \quad (15)$$

where \mathbf{u}_{rel} denotes the relative velocity between the droplet and the surrounding gas and d_d is the particle diameter. Also, C_D stands for the drag coefficient and is computed via the following correlation for the standard drag curve on a smooth sphere; see, for example, [24],

$$C_D = \begin{cases} \frac{24}{Re_d} (1 + \frac{1}{6} Re_d^{\frac{2}{3}}) & Re_d < 1000, \\ 0.424 & Re_d \geq 1000. \end{cases} \quad (16)$$

In this expression, Re_d is the droplet Reynolds number, i.e. the Reynolds number based on the relative velocity, liquid radius and gas viscosity.

The contribution of the other forces acting on the droplets, such as the virtual mass, Faxen, Basset, Magnus and Saffman forces, are considered negligibly small and are neglected. This is a common practice in simulation of sprays [15].

Liquid evaporation is taken into account by the evaporation model of Amsden et al. [2] which assumes that the fuel droplets are spherical and have uniform properties in their interior. This assumption is justified if the droplet Biot number is less than unity [16], which is the case in the present study.

The energy balance for a single droplet, neglecting the radiation and the kinetic energy related to the mass evaporated, is given by

$$m_d c_{p,d} \frac{dT_d}{dt} = Q_d + \dot{m}_d h_1. \quad (17)$$

Herein T_d is the droplet temperature (assumed constant in the interior of a droplet), $c_{p,d}$ is the specific heat of the liquid, h_1 the latent heat of evaporation of the fuel and m_d the droplet mass. The first term on the right-hand side of the above equation, Q_d , represents the convective and conductive heat transfer between droplet and surrounding gas, while the second term stands for the latent heat of vaporization. In our study Q_d is approximated by,

$$Q_d = \kappa_d \pi d_d (T - T_d) Nu. \quad (18)$$

In other words, we assume that Q_d is proportional to the temperature difference between the two phases. In equation (18), κ_d stands for thermal conductivity of the droplet and Nu is the Nusselt number. For the case of spherical droplets, the Nusselt number is estimated via the following correlation of Ranz and Marshall [35,36],

$$Nu = 2 + 0.6\sqrt{Re_d}\sqrt[3]{Pr}, \quad (19)$$

where Pr is the Prandtl number with respect to the liquid and Re_d is the Reynolds number of the droplet.

The evaporation rate of a droplet \dot{m}_d is written as,

$$\dot{m}_d = \frac{1}{2}\pi\rho_d d_d^2 \frac{dd_d}{dt}, \quad (20)$$

where d_d stands for the droplet diameter and its rate of decrease is approximated via the solution of the Stefan problem in spherical coordinates,

$$\frac{dd_d}{dt} = -\frac{2\rho D}{\rho_d d_d} \frac{Y_{f,s} - Y_{f,\infty}}{1 - Y_{f,s}} Sh. \quad (21)$$

In (21), $Y_{f,s}$ denotes the at the droplet surface, $Y_{f,\infty}$ denotes the mass fraction of the fuel vapor in the free stream, and D is the mass diffusivity of the fuel with respect to nitrogen, the dominant species of the gaseous phase. Finally, Sh is the Sherwood number with respect to the droplet and can be approximated by a correlation that is equivalent of the one above for Nu [36], i.e.

$$Sh = 2 + 0.6\sqrt{Re_d}\sqrt[3]{Sc}, \quad (22)$$

where Sc is the droplet Schmidt number. With these expressions, one can solve (21) for the new droplet radius and then (17) for the new droplet temperature.

3 Secondary Breakup Models

In the problem of interest, the operating conditions are such that both primary breakup and atomization occur very close to the nozzle exit and for this reason they are not included in our study. Instead, we consider a pre-atomized spray. We further assume that collisions between droplets occur very rarely and can therefore be ignored. Our study focuses on the simulation of the secondary breakup. To this end, three different models for secondary breakup are tested, namely, the Taylor Analogy Breakup [30], the Reitz-Diwakar [39] and the Pilch-Erdman [34] models. In what follows these models are briefly reviewed.

3.1 Taylor Analogy Breakup (TAB) model

This model, first suggested by O'Rourke and Amsden [30], is based upon the analogy between a second-order harmonic oscillator, i.e. a forced Mass-Spring-Damper (MSD) system, and a fuel droplet that moves through a gas. According to this analogy, the aerodynamic drag plays the role of the external force f which deforms the droplet, thereby initiating its oscillation. Further, surface tension acts as a restorative force that tries to maintain the sphericity of the droplet and to minimize its deformation. Therefore, in the MSD system, the surface tension plays the role of the spring force kx where x is the displacement of the droplet equator from its undisturbed position. The viscous stresses due to the motion of the liquid inside the droplet are of dissipative nature and play the role of the damping force $b dx/dt$. The second order differential equation of the MSD system is then formulated as,

$$m_d \frac{d^2 x}{dt^2} = -b \frac{dx}{dt} - kx + f, \quad (23)$$

where m_d is the mass of the droplet.

The TAB model keeps track only of the fundamental mode of oscillation, which corresponds to the lowest order harmonic whose axis is aligned with \mathbf{u}_{rel} . At small Weber numbers this mode is dominant, whereas at large Weber numbers other modes have significant contributions to droplet breakup. As mentioned in the Introduction, the Weber number We is the ratio between inertial force and surface tension, $We = (\rho \mathbf{u}_{\text{rel}}^2 r_d) / \sigma$.

In accordance with the Taylor analogy [30], the physical dependencies of the coefficients in the equation are the following.

$$\frac{f}{m_d} = C_f \frac{\rho |\mathbf{u}_{\text{rel}}|^2}{\rho_d r_d}, \quad \frac{k}{m_d} = C_k \frac{\sigma}{\rho_d r_d^3}, \quad \frac{b}{m_d} = C_b \frac{\mu_d}{\rho_d r_d^2}, \quad (24)$$

where r_d is the radius of the droplet, σ is the gas-liquid surface tension, μ_d is the viscosity of the liquid fuel and, C_f , C_k and C_b are dimensionless coefficients.

Additionally, the displacement of the droplet is nondimensionalized according to $y = x / (C_r r)$ where C_r is a scaling dimensionless constant. By substituting these expressions, the equation of the harmonic oscillator (24) can be written as,

$$\frac{d^2 y}{dt^2} = \frac{C_f}{C_r} \frac{\rho}{\rho_d} \frac{|\mathbf{u}_{\text{rel}}|^2}{r_d^2} - C_k \frac{\sigma}{\rho_d r_d^3} y - C_b \frac{\rho_d \mu_d}{r_d^2} \frac{dy}{dt}. \quad (25)$$

According to O'Rourke and Amsden [30], breakup occurs when the dimensionless displacement y becomes equals to unity. Then, the values of the constants C_f , C_k , C_b and C_r are calculated by employing a combination of experimental and theoretical results. More specifically, C_k and C_b are obtained by matching the fundamental oscillation frequency and the oscillation of the fundamental mode for the damping coefficient. Accordingly, they take the following values, $C_k = 8$ and $C_b = 5$ [22]. Also, in the TAB model is it assumed

that breakup occurs if and only if the amplitude of the oscillation of the north and south poles of the droplet become equal the droplet radius. From this assumption, and since $y = 1$ during breakup, we have that

$$C_r = \frac{1}{2}. \quad (26)$$

Further, according to experiments [28], the critical Weber number (We_{cr}) for breakup was found to be $We_{cr} = 6$. According to O'Rourke and Amsden [30], the model matches the experimental results if

$$\frac{C_k C_r}{C_f} = 2We_{cr} = 12. \quad (27)$$

By inserting (26) into (27), we arrive at

$$C_f = \frac{1}{3}. \quad (28)$$

With regard to the atomization characteristics, O'Rourke and Amsden [30] suggest that the equation of the droplet size after breakup should be based on the energy conservation between the parent droplet and the product droplets by combining the droplet oscillation energy and surface energy.

We further note that, in reality, any ensemble of droplets will be polydisperse. The Sauter Mean Diameter (SMD), r_{32} , is defined as the droplet size in a monodisperse ensemble for which the total surface energy is equal to the total surface energy of an ensemble of polydisperse droplets when both ensembles have the same total area and total volume [40]. In the TAB model, the relation between the radius of the parent droplet r_d and the SMD r_{32} of the product droplets reads,

$$\frac{r_d}{r_{32}} = 1 + \frac{8K}{20} + \frac{\rho_d r_d^3}{\sigma} \left(\frac{dy}{dt} \right)^2 \left(\frac{6K - 5}{120} \right). \quad (29)$$

In (29) the value of K is obtained via comparisons with experimentally measured droplet sizes, and is set to $K = \frac{10}{3}$. After breakup, the radius of the product droplets is chosen randomly from a χ^2 distribution, and the number of droplets is computed so as to satisfy mass conservation.

3.2 Reitz-Diwakar (RD) model

The RD model [39] is based on the correlations given by Nicholls [28] where two different breakup regimes are identified with respect to the Weber number. Bag breakup occurs when $We > We_{cr}$ and stripping breakup when

$$We > C_{s1} \sqrt{Re_d}, \quad (30)$$

where C_{s1} is an empirically determined constant whose value is set at $C_{s1} = 0.5$. Similarly to the TAB model, the RD model also assumes that $We_{cr} = 6$.

With regard to the breakup regime, both breakup time and the stable diameter of new droplets are calculated.

The size of the unstable droplet varies with time according to the following rate equation,

$$\frac{dr_d}{dt} = \frac{(r_{st} - r_d)}{t_{br}}, \quad (31)$$

where r_d is the droplet radius prior to breakup, r_{st} is the new radius for the stable droplet and t_{br} is the characteristic breakup time. Once the droplet radius reduces to r_{st} , the droplet is considered to be stable and does not disintegrate further. The number of droplets in each parcel after the breakup is determined from the mass conservation within the parcel. The characteristic breakup time and stable radius for each breakup regime are calculated as follows,

Bag breakup:

$$t_{br} = C_1 \sqrt{\frac{\rho_d r_d^3}{2\sigma}}, \quad r_{st} = \frac{6\sigma}{\rho |\mathbf{u}_{rel}|^2}. \quad (32)$$

Stripping breakup:

$$t_{br} = C_2 \frac{r_d}{|\mathbf{u}_{rel}|} \sqrt{\frac{\rho_d}{\rho}}, \quad r_{st} = \frac{\sigma^2}{2\rho^2 |\mathbf{u}_{rel}|^3 \nu}. \quad (33)$$

In the above expressions C_1 and C_2 are also empirically determined constants and their values are set at $C_1 = \pi$ and $C_2 = 20$.

3.3 Pilch-Erdman (PE) model

According to this model, the droplet deformation and breakup times are calculated from the experimental data of Pilch and Erdman [34] and Hsiang and Faeth [17] for the maximum size of stable fragments. The model makes a distinction between the various observed mechanisms of droplet breakup; i.e. vibrational breakup, bag breakup, streamer breakup, striping breakup and catastrophic breakup. This classification is based on observations of droplet breakup.

The PE model is based on the assumptions that droplet breakup occurs only if the droplet Weber number is greater than a critical value. Brodkey and Addison [5] introduced the following empirical correlation for gas-liquid systems,

$$We \geq 6(1 + 1.077(Oh)^{1.6}), \quad (34)$$

where Oh is the Ohnesorge number; as mentioned in the Introduction, it is defined by $Oh = \mu_d / \sqrt{\rho_d d_d \sigma}$.

The droplet breakup process is therefore categorized into different regimes depending on the droplet Weber number. The characteristic dimensionless

time of the droplet breakup due to Rayleigh-Taylor and Kelvin-Helmholtz instabilities is given by:

$$t_{\text{br}} = t \frac{|\mathbf{u}_{\text{rel}}|}{d_{\text{d}}} \sqrt{\frac{\rho}{\rho_{\text{d}}}}. \quad (35)$$

The total breakup time t_{br} is defined as the time when the droplet and its fragments no longer undergo further breakup. The following correlation for total breakup time are provided [34],

$$t_{\text{br}} = \begin{cases} 6(2We - 2We_{\text{cr}})^{-0.25}, & We_{\text{cr}} \leq We \leq 9, \\ 2.45(2We - 12)^{0.25}, & 9 \leq We \leq 22.5, \\ 14.1(2We - 12)^{0.25}, & 22.5 \leq We \leq 175.5, \\ 0.766(2We - 12)^{0.25}, & 175.5 \leq We \leq 1335, \\ 5.5, & 1335 \leq We. \end{cases} \quad (36)$$

In these expressions, the Weber number We has been multiplied by a factor of 2 because the Weber number in [34] We is defined on the basis of the droplet diameter instead of the droplet radius. When the Ohnesorge number Oh is small, i.e. $Oh < 0.1$, then $We_{\text{cr}} = 6$, which is the value used in our study.

After breakup, the new stable diameter is obtained by accounting for fragment size reduction and decreasing relative velocity,

$$d_{\text{d}} = 2We_{\text{cr}} \frac{\sigma}{\rho v^2} \left(1 - \frac{|\mathbf{u}_{\text{d}}|}{|\mathbf{u}_{\text{rel}}|}\right)^{-2}, \quad (37)$$

where, \mathbf{u}_{d} is the velocity of the fragment cloud when all breakup processes cease. Its amplitude is calculated from the following relation [33],

$$\frac{|\mathbf{u}_{\text{d}}|}{|\mathbf{u}_{\text{rel}}|} = \sqrt{\frac{\rho_{\text{d}}}{\rho}} \left(\frac{3}{4}C_{\text{w}}t_{\text{br}} + 3Bt_{\text{br}}^2\right), \quad (38)$$

where the coefficients C_{w} and B are set equal to,

$$C_{\text{w}} = 1, \quad B = 0.116. \quad (39)$$

4 Modified Taylor Analogy Breakup (MTAB) model

In this section we propose a modification to the original TAB model. At high We , the aerodynamic force f plays a dominant role in the disintegration of the droplet. According to the original model, the coefficient C_f , which incorporates the effect of the external forces, is determined empirically.

Herein, we propose to calculate C_f dynamically for each droplet. More specifically, since f represents the aerodynamic drag, C_f can be cast as a function of the drag coefficient of the sphere C_{D} . Due to the fact that the

droplet diameters are small, we may approximate the frontal area of a droplet by that of a perfect sphere with the same diameter. Therefore, we can write:

$$\frac{f}{m_d} = \frac{1}{2} \frac{\rho A_d |\mathbf{u}_{\text{rel}}|^2 C_D}{V_d \rho_d} = \frac{3}{4} C_D \frac{\rho |\mathbf{u}_{\text{rel}}|^2}{\rho_d d_d}, \quad (40)$$

where A_d and V_d denote the frontal area and volume of the droplet, respectively. Also, in the above expression the drag coefficient C_D is computed via the correlation (16).

By combining (40) and the first relation in (24), we readily arrive in the following relation between C_f and C_D ,

$$C_f = \frac{3}{8} C_D. \quad (41)$$

Following the analysis of the TAB model, the remaining values of constants, C_r and C_b are kept as before, while the value of the C_k is calculated dynamically using (27) and (40). Also the diameters of the droplets after breakup are calculated as in the TAB model, namely, by employing relation (29). According to the proposed modification, the parameters entering the equation for the harmonic oscillator (25) have different values for each droplet, based on the droplet characteristics and local flow conditions.

Finally, with regard to breakup modelling, it is important to mention that the evolution of the droplets, including breakup, is also affected by the turbulent motion of the ambient gas [41]. This is taken into account into the droplet equation of motion (15) and the afore-mentioned secondary breakup models since they involve the fluid velocity. Nonetheless, these models do not take explicitly into account the turbulence properties. On the other hand, the model in [41] does include the effect of turbulence on secondary atomization. However, to our knowledge, the model in [41] and related ones are based on a priori knowledge of the turbulence properties. Most often, this information is not available; this is also the case in our simulations. In fact, in our study the jet is injected in still gas and turbulence is induced by the motion of the droplets. Therefore, in our study it is not possible to know a priori the properties of the gas turbulence so as to include it in the breakup modelling.

5 Numerical results and discussion

5.1 Computational setup

As mentioned in the Introduction, numerical simulations have been carried out under a set of prescribed conditions that is referred to as Spray A by the Engine Combustion Network (ECN) [9]. Experimental results of Spray A have been obtained from the SANDIA National Laboratories through the ECN [10], and have been chosen as a reference for comparison in this study. Liquid n-dodecane is injected through a 90 μm diameter nozzle into a stationary gas whose temperature is 900 K and initial density is 22.8 kg/m^3 . The initial

velocity of the droplets is calculated from the injected mass flow rate that is provided by the experiments and shown in Figure 1, while the injection direction is chosen randomly.

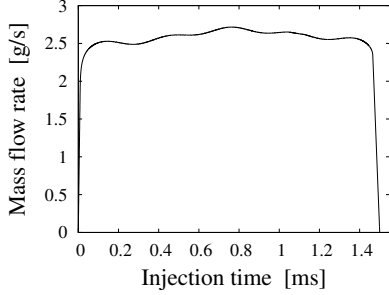


Fig. 1: Profile of mass flowrate of fuel. The injection starts at $t = 0$ and terminates at $t = 1.5$ ms.

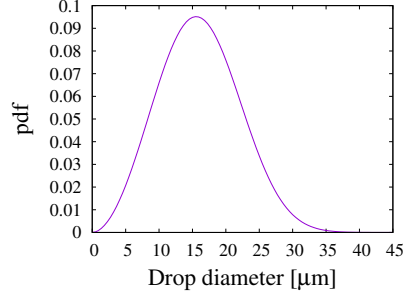


Fig. 2: Rosin-Rammler distribution for the initial diameter of the droplets.

Initially, the molar composition of the gas is, $N_2 = 89.71\%$, $CO_2 = 6.52\%$ and $H_2O = 3.77\%$ [10]. Herein we examine a flow without chemical reactions, so the concentration of O_2 is always zero. The various thermophysical properties of both fuel and surrounding gas vary significantly within the temperature range considered in our study. Their values are computed via the well-known 9th-order polynomial correlations developed by NASA [6]. For example, the latent heat of vaporization of n-dodecane in the range of 299 – 446 K varies between 51.60 and 65.70 kJ/mol. Also, in our study we assume uniform physical properties inside each liquid fuel droplet. Moreover, the initial thermodynamic conditions for our simulations, are listed in Table 1.

Table 1: Case details.

Spray details	
Fuel	n-dodecane ($C_{12}H_{26}$)
Fuel temperature [K]	363
Fuel density [kg/m^3]	643
Nozzle diameter [μm]	90
Injection pressure [MPa]	150
Nominal injection velocity [m/s]	550
Injection duration [ms]	1.5
Injected fuel mass [mg]	3.5
Ambient conditions	
Temperature [K]	900
Density [kg/m^3]	22.8
Pressure [MPa]	6

The amount of injected parcels over the duration of the simulation is set to 1 200 000. With regard to the properties of the droplets at the injection position, we remark the following. As mentioned in the Introduction, Faeth et al. [12], the geometry of the nozzle has a direct impact on the atomization of the liquid jet (i.e. the primary breakup), including the sizes of the formed droplets. This, in turn, affects the secondary atomization. In our simulations we have followed a common procedure which is to adopt a stochastic approach for the droplet properties at the injection position. More specifically, as mentioned above, the position and velocity direction of each parcel are chosen in a random fashion, whereas the velocity amplitude at injection is chosen so as to match the mass-flow rate of the corresponding experiments.

Further, the droplet diameter is determined via a presumed probability distribution function. In our simulations we employed the Rosin-Rammler distribution [48,43]. This is a popular choice for spray simulations and its appropriateness has been established in [23]. The Rosin-Rammler distribution is described by two parameters. The first parameter corresponds to the droplet size distribution parameter q ; herein we followed the recommendations in [23] and set $q = 3$. The second one is the characteristic diameter of the distribution D ; in our study it is calculated so as the SMD matches a prescribed value. In turn, the prescribed value of the SMD is calibrated so as to match the experimental data for the liquid penetration distance, thereby taking into account the effects of the nozzle geometry and the details of the primary breakup. The resulting distribution for the initial droplet diameter is shown in Figure 2. For the numerical implementation of the Rosin-Rammler distribution we followed the procedure described in [1]. Finally, density and temperature of the droplets at the injection position are set equal to the given density and temperature of the fuel jet.

The computational domain is a cuboid with a cross-flow section equal to 20 mm \times 20 mm and streamwise length equal to 80 mm. Further, the computational domain is assumed to be adiabatically isolated. In order to improve the computational accuracy, an adaptive mesh refinement with 3 levels of refinement is implemented based on the fuel vapor fraction. This results in a mesh composed of 2.1 million cells. The size of the largest cell is 0.4 mm while the size of the smallest one is 0.05 mm. The smallest cells are clustered close to the injection position. Figure 3 shows the dynamic evolution of the mesh.

In our simulations, we use a variable time-step with the CFL number set to 0.3. Initially, the droplets are injected in still gas. The injection of the liquid fuel stops at $t = 1.5$ ms. The fuel evaporation is completed at approximately 1.6 ms. Since we did not know a priori the required time for evaporation of the injected fuel, we stopped our early simulations at $t = 2$ ms so as to ensure that the fuel has been completely evaporated.

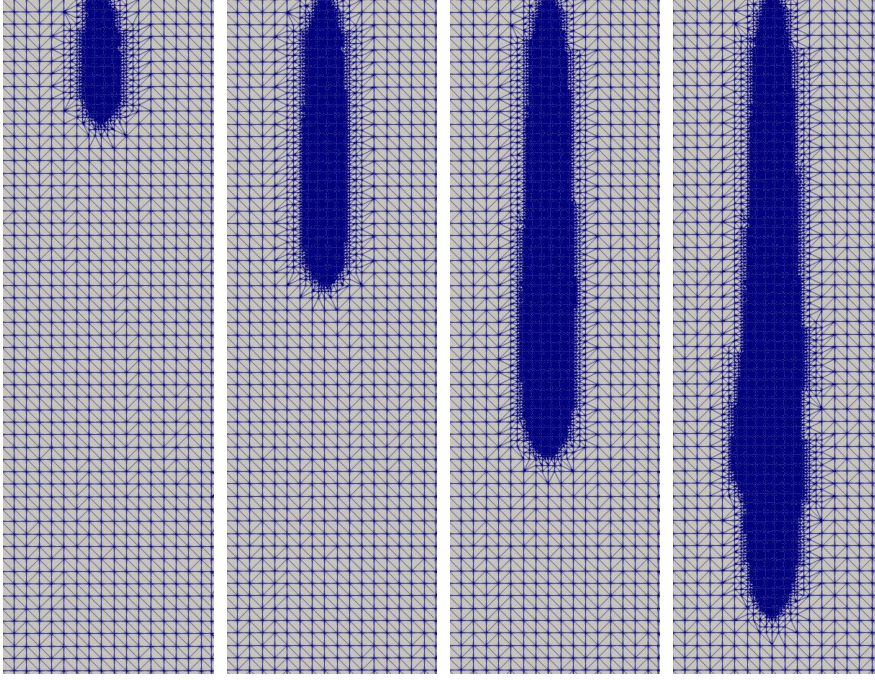


Fig. 3: Resulting dynamic mesh refinement based on vaporized fuel fraction at $t = 0.02, 0.05, 0.075$ and 0.1 ms.

5.2 Numerical Results and Discussion

The global quantities against which we will compare our simulations are liquid penetration and vapor fuel penetration distance. We also present the computed Probability Distribution Function (PDF) of the droplet diameter in different regions of the computational domain and discuss further some characteristics of the spray. First, we compare the TAB, RD and PE models against experimental data, and the most accurate model is compared to the MTAB model. The experimental data for the liquid penetration distance are obtained via high-speed Mie-scattering imaging using a 3% threshold of maximum intensity. The experimental data for the vapor penetration distance are extracted via shadowgraph or schlieren imaging. Additionally, the experimental data for the liquid penetration distance are the average values from an ensemble of 20 injections [32].

5.2.1 Liquid penetration distance

The liquid penetration distance is defined as the axial distance between the injection position and the farthest control volume at which the liquid volume

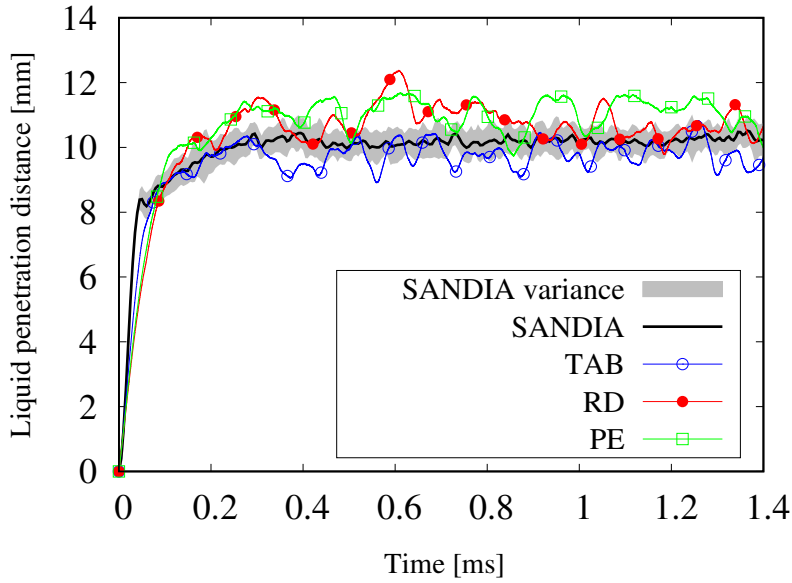


Fig. 4: Liquid penetration distance predicted by the three different models along with experimental results (SANDIA).

fraction is reduced to 0.1%. This control volume is a cylinder of 1 mm diameter and 1 mm axial length [9].

Figure 4 depicts plots of the liquid penetration distance against time, computed via the TAB, RD and PE models. In this figure we also show the experimental data of SANDIA Spray A and their variance (error bars). According to the spray A operating conditions of ECN [10], the spray injection starts to drop rapidly at $t = 1.4$ ms and terminates at $t = 1.5$ ms. However, in the experiments, the fuel injection continues after 1.5 ms. Since the injection flowrate in the simulations differs from that of the experiments after $t = 1.4$ ms, herein we provide results for the liquid penetration distance only up to $t = 1.4$ ms.

From Figure 4 three distinct phases of the spray evolution can be identified. In the first phase, from the beginning of the injection until 0.07 ms, there is a rapid increase in fuel penetration distance up to 7-8 mm. During this phase the liquid penetration is mainly influenced by the initial velocity and direction of the parcels. In other words, during this early phase, the droplets behave in a ballistic manner. Further, the droplet evaporation rate is kept small and does not significantly affect the liquid penetration distance. This can be corroborated by the small values of the fuel vapor mass fraction in the region close to the injection point, as shown in Figure 5. Also in this stage droplets lose most of their momentum to gas phase acceleration.

In the second phase, which ranges from approximately 0.1 ms until 0.25 ms, the increase in liquid penetration distance begins to slow down until. Finally in

the third phase, from 0.25 ms onwards, the liquid penetration distance remains nearly constant and equal to approximately 10 mm. This fact implies that the droplets evaporate completely within this value of the liquid penetration distance (10 mm). This third and final phase of the evolution of the spray is referred to herein as the “stationary”, in the sense that the liquid penetration distance no longer increases with time. During this phase, fuel evaporation plays a dominant role because it reduces the size of the droplets.

Figure 5 shows contour plots of the fuel mass fraction with time. As we can see, at any given instance, the fuel mass fraction increases with the distance from the injection position. This is to be expected since it implies that evaporation is intensified downstream. Further, in Figure 6 we provide contour plots of the temperature field. Upon comparison of the images shown in Figures 5 and 6, we infer that as the spray evolves, the flow of the surrounding gas becomes turbulent, thereby enhancing the mixing process.

According to our simulations, the RD and PE models globally overpredict the liquid penetration distance. Moreover, they underestimate the rate of increase of the liquid penetration distance during the first phase. By contrast, the TAB model captures more accurately the liquid penetration distance during

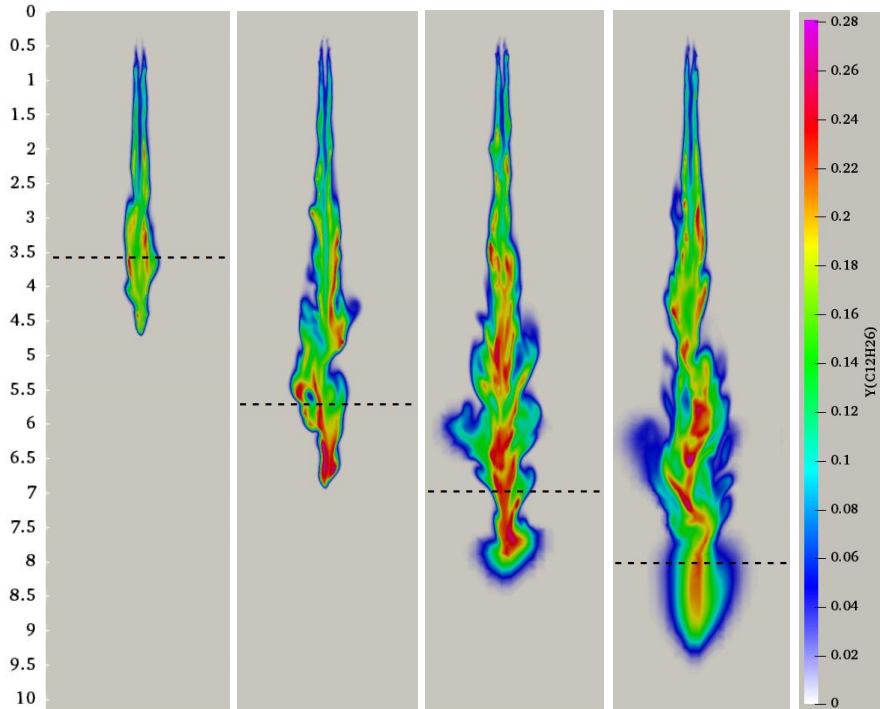


Fig. 5: Fuel vapor mass fraction near the injection point, computed via the TAB model, at times $t = 0.02, 0.05, 0.075$ and 0.1 ms. The horizontal dashed line shows the location of the liquid penetration distance.

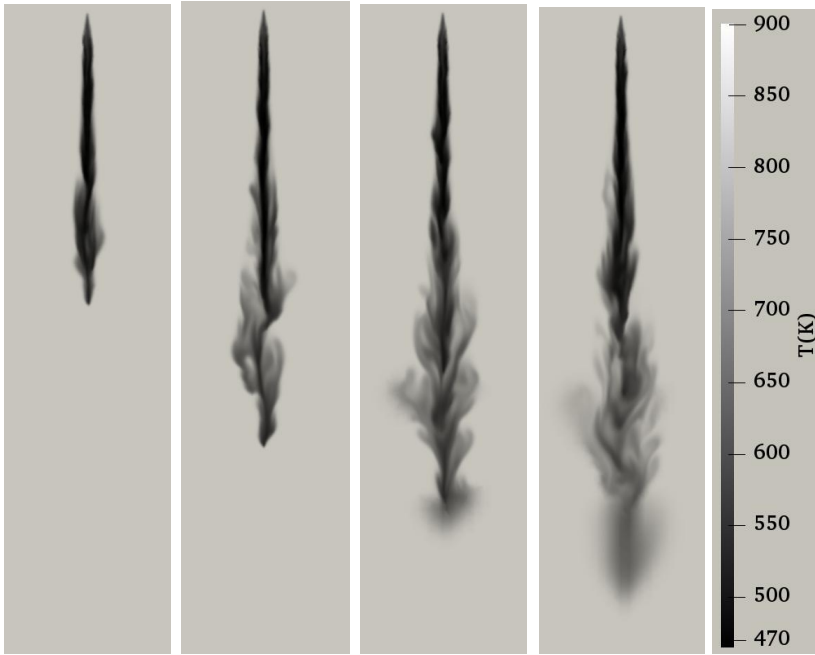


Fig. 6: Temperature field near the injection point at times $t = 0.02, 0.05, 0.075$ and 0.1 ms. The results shown herein are taken from a simulation with the TAB model.

the first phase. Also, it slightly underpredicts this distance during the third stationary phase. This is because the TAB model accounts for the velocity-dependent droplet oscillations, which tends to accelerate the disintegration of the droplets and, consequently, leads to faster evaporation.

For the flow conditions of our study, the predictions for the liquid penetration distance from the TAB model are slightly more accurate than those of the RD and PE models. Nonetheless, with all three models, the fluctuations in the liquid penetration distance during the stationary phase have higher magnitude than in the experimental results. This may be attributed to the relatively small number of parcels that are injected during the whole simulation. A secondary factor that may contribute to this discrepancy is the different sampling frequency between experimental measurements and numerical simulations; in our study, the liquid penetration distance is evaluated at each time step, whereas the sampling frequency in the experimental was lower. For these reasons, some peaks in the oscillations of the liquid penetration distance might have been missed in the measurements.

In Figure 7 we have plotted the liquid penetration distance, as predicted by the TAB and MTAB models along with the experimental results of SANDIA. The results for the liquid penetration distance shown in Figure 4 and 7 are

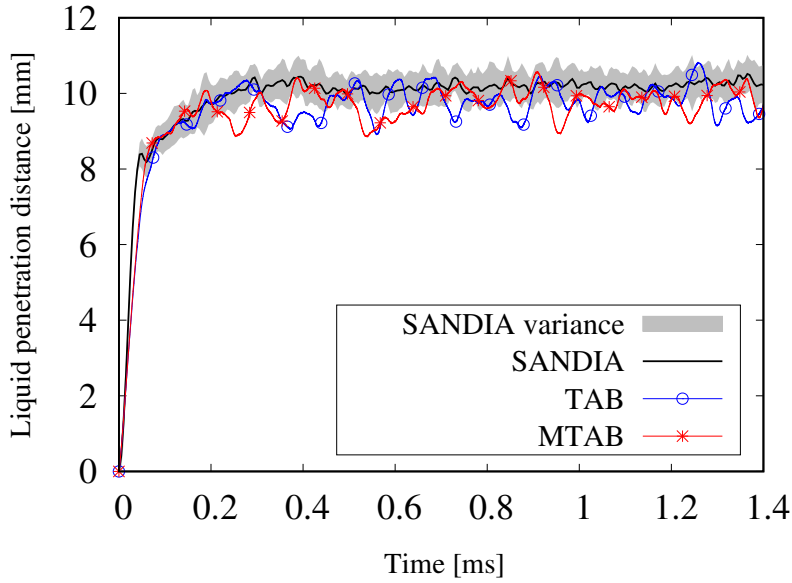


Fig. 7: Liquid penetration distance predicted by TAB and MTAB models along with experimental results (SANDIA).

presented separately for lisibility purposes. From this figure we see that the differences between the prediction of the TAB and MTAB are small especially for the third phase of the evolution of the spray. This is to be expected because these models have been calibrated so as to match the liquid penetration distance. Nonetheless, we can see that the proposed MTAB model yields more accurate results during the first and second phases.

In Table 2 we provide the values of the Mean Absolute Error (MAE) in the computation of the liquid penetration distance with all four models considered herein. The MAE is defined by,

$$\text{MAE} = \frac{1}{t_n - t_0} \sum_{i=1}^{i=n} |N(t_i) - E(t_i)| \Delta t_i, \quad (42)$$

where N_i ($i = 1, \dots, n$) are the numerical results, E_i are the experimental results and t_i are the time instances that these results are registered. The MAE

Table 2: Mean Absolute Error with different models [mm].

Breakup model, 1.2×10^6 parcels	RD	PE	TAB	MTAB
Liquid penetration distance	0.7	0.91	0.46	0.44
Vapor penetration distance	10.1	11.4	10.6	7.8

for the liquid penetration length is calculated on the basis of the results for the third phase of the spray evolution and, more specifically, between $t_0 = 0.2$ ms and $t_n = 1.4$ ms. On the basis of these data, we conclude that the MTAB model gives slightly better results for the liquid penetration distance, compared to the results with the other three models.

In terms of repeatability of the results, we have run several realizations of the numerical simulations with the MTAB model, each time with a different sequence of random values for the initial diameter, coordinates and velocity direction of the parcel at the injection position. The numerical predictions of different realizations exhibited a variance of approximately 3.7%.

Finally, in terms of numerical convergence, we conducted numerical simulations with the MTAB model and different number of parcels with liquid droplets (namely, 0.75×10^6 , 1.2×10^6 and 1.7×10^6 number of parcels). The MAE of these simulations are summarized in Table 3. From this table we readily infer that numerical convergence with regard to the number of parcels is achieved, in the sense that successive increases of the number of parcels lead to successively less improvement in terms of the MAE. Moreover, on the basis of these results, we may infer that the nominal number of parcels, 1.2×10^6 parcels, is deemed satisfactory for the purposed of our study.

5.2.2 Vapor penetration distance

The vapor penetration distance is defined as the axial distance between the injection position and the tip of the vapor fuel plume, at which the mass fraction of the vapor fuel is 0.1% [9]. Figure 8 depicts the evolution of the vapor penetration distance as predicted by the four models considered in our study, together with the experimental data of SANDIA [10] and IFPEN [19].

In Figure 8 we plot the numerical results obtained via the TAB, RD, PE and MTAB models, along with the experimental results of SANDIA and IFPEN. As mentioned above, according to the protocol for Spray A simulations, the injection stops at $t = 1.5$ ms whereas in the experiments it continues after this time. Because of this difference in the injection, the numerical results will be significantly different from the experimental ones after a certain time, approximately $t = 1.7$ ms. In other words, the termination of the injection at $t = 1.5$ ms will start impacting the vapor penetration distance at approximately $t = 1.7$ ms. For this reason, in Figure 8 we have plotted results up to $t = 1.7$ ms.

In this figure, we observe that during the third “stationary” phase of the spray evolution, the vapor penetration distance increases with time at an al-

Table 3: Mean Absolute Error with MTAB [mm].

Number of parcels	0.75×10^6	1.2×10^6	1.7×10^6
Liquid penetration distance	0.63	0.44	0.39
Vapor penetration distance	8.64	7.8	7.7

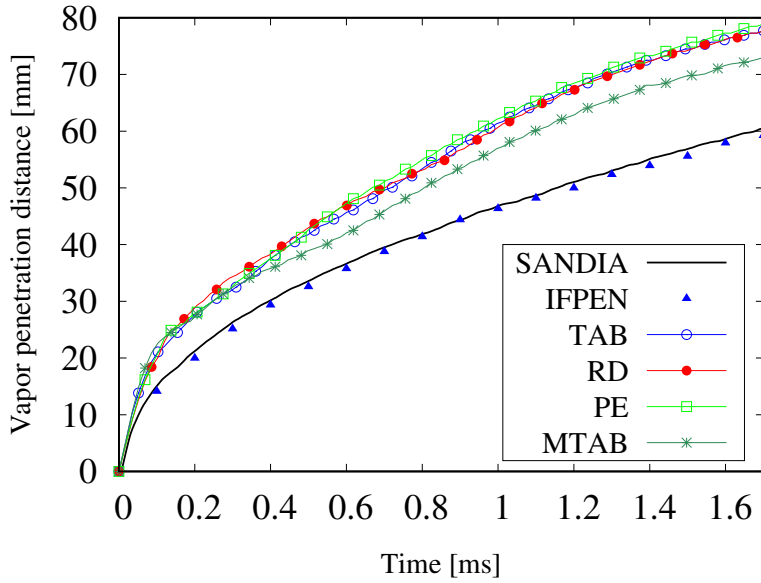


Fig. 8: Vapor penetration distance predicted by different models along with experimental results of SANDIA and IFPEN.

most constant rate. In other words, it increases almost linearly with time. In particular, these models predict an almost linear profile, but they overpredict the rate of increase. This leads to significant discrepancies between the numerical results and the experimental data.

We also note that the differences between the predictions with the TAB, RD and PE models are very small. On the other hand, the MTAB model also overpredicts the vapor penetration distance but to a lesser degree than the other models. The MAE in the computation of the vapor penetration distances with the different models is given in Table 2. The MAE for the liquid penetration length is calculated on the basis of the results for the third phase of the spray evolution and, more specifically, between $t_0 = 0.2$ ms and $t_n = 1.7$ ms; see (42).

According to the data provided in this table, the MAEs of the three pre-existing models tested herein are comparable, whereas the MAE of the MTAB model is approximately 20% smaller. In other words, the MTAB model provides a mild improvement over the pre-existing models.

The discrepancies between numerical and experimental results are primarily attributed to the shortcomings of the breakup models. Another factor that also contributes to these discrepancies is the LES model, which does not resolve all turbulent scales and the evaporation model which assumes uniform temperature inside the droplet thereby leading to a higher evaporation rate. Finally, one could argue that the observed discrepancy is also due to errors in the mea-

surement of the vapor penetration distance. However, as can be inferred from Figure 8, the data obtained from two different experimental studies, SANDIA and IFPEN, are very close. Therefore, we argue that it is rather unlikely that experimental errors contribute to the observed discrepancy between numerical predictions and experimental data.

As regards comparisons with simulations via Eulerian-Eulerian modeling we remark the following. The results in [25] show better agreement with experiments; however those results have been obtained on a mesh 15 million cells, whereas the mesh in our simulations is only 2 million cells. On the other hand, the simulations in [21, 47] were conducted with mesh sizes comparable to ours; the simulations produced more accurate results for the vapor penetration distance but less accurate results for the liquid penetration distance. Overall, the results reported in [21, 47] have the same level of agreement with experiments as our results that were obtained via an Eulerian-Lagrangian approach.

Finally, it is worth noting that the MAE in the prediction of the vapour penetration distance with the MTAB and different number of parcels is given in Table 3. As mentioned above, numerical convergence with regard to the

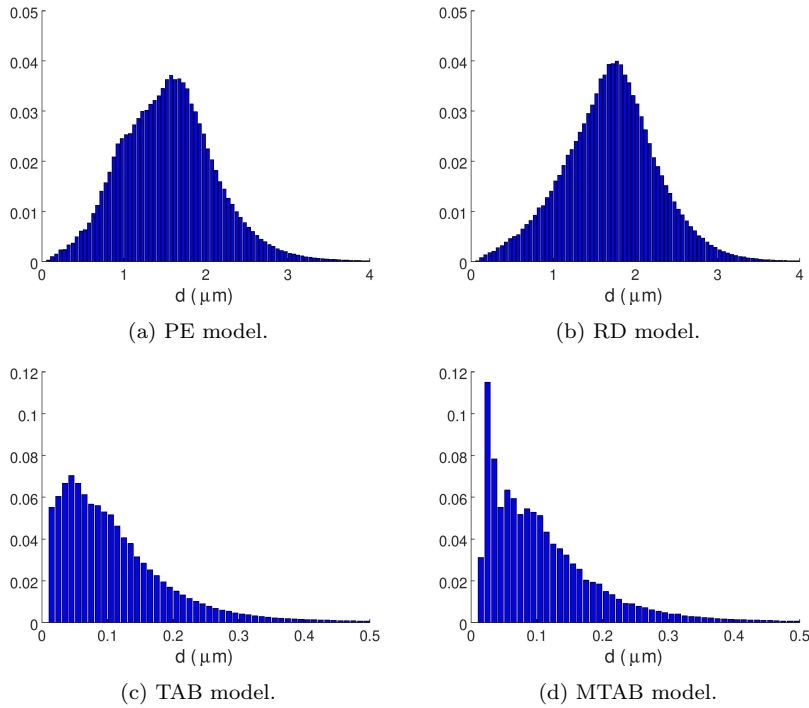


Fig. 9: PDFs of droplet diameters for the four breakup models considered in our study.

number of parcels is achieved, in the sense that successive increases of the number of parcels lead to successively less improvement in terms of the MAE.

5.2.3 Droplet diameter PDFs

In this section we examine the impact of the secondary breakup models on the PDFs of the droplet diameters. For this purpose we average the droplet diameter values over 9 different instances, namely $t = 0.1, 0.2, \dots, 1$ ms. All these instances are in the third, “stationary”, phase of the spray evolution.

Figure 9 shows the computed PDFs of the droplet diameter by taking into account the droplets in the entire computational domain. We observe that the RD and PE models have the same magnitude of droplet diameters. The same is true for the TAB and MTAB models but the magnitude is considerably smaller than that of the PE and RD models.

The TAB and MTAB models predict significantly smaller droplet diameters; in fact, they predict diameters that are approximately 20 times smaller than those predicted by the RD and PE models. This is due to the different

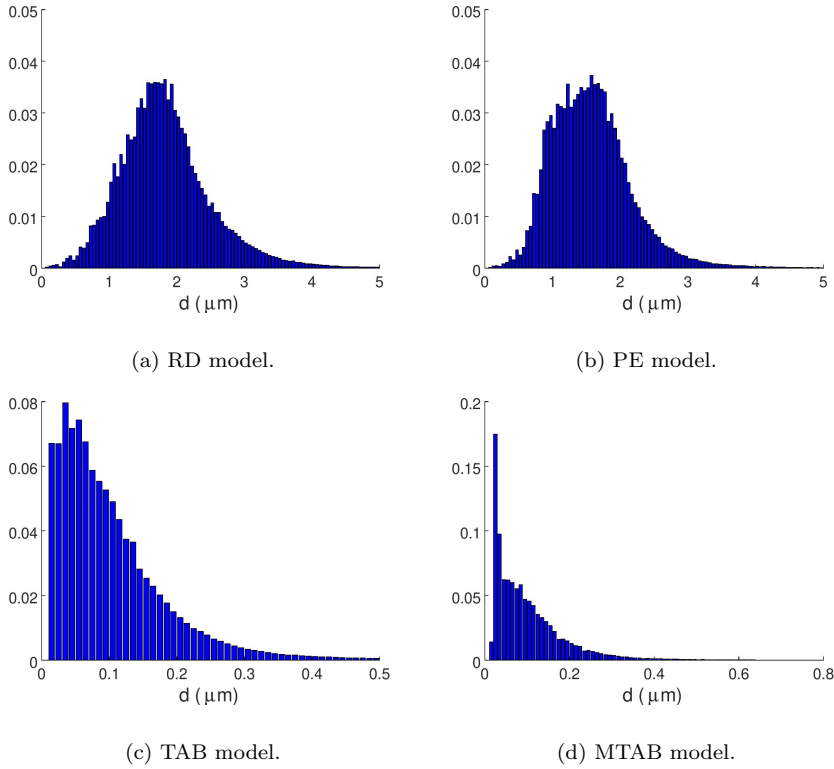


Fig. 10: PDFs of droplet diameters in Control Volume 1 for the four breakup models considered in our study.

approaches in the computation of the droplet diameter after breakup. More specifically, in the TAB and MTAB models, the diameter of the droplets after breakup is chosen randomly from a χ -square distribution with a SMD resulting from relation (29). Consequently, the diameter of the new droplets could be of any size. It turns out that such a stochastic method for computing the diameters of newly formed droplets produces more realistic results.

Further, although the initial PDF of the droplet diameter follows the Rosin-Rammler distribution, the computed distributions from the RD and PE models are markedly different from the Rosin-Rammler distribution and do not preserve its skewness. On the other hand, the computed distributions from the TAB and MTAB models are significantly more skewed and tend to resemble more a Rosin-Rammler distribution. Again, this is attributed to the stochastic method used to set the droplet diameters after breakup. Additionally, in Figure 9(d) a peak of small droplets can be observed. We attribute this peak to the fact that the MTAB model predicts shorter droplet lifespan than the standard TAB does.

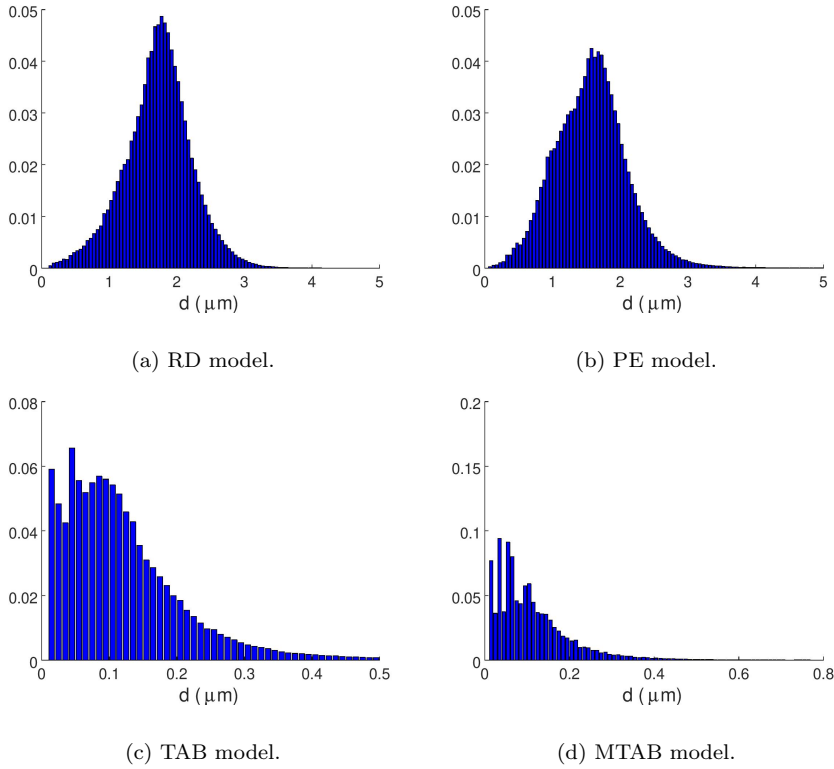


Fig. 11: PDFs of droplet diameters in Control Volume 2 for the four breakup models considered in our study.

Figure 10 depicts the droplet diameter PDFs inside a cylindrical control volume of radius 1 mm and height of 6 mm. This control volume is aligned with the symmetry axis of the spray and located close to the injection position so as to include the region covered by the spray. Herein, it is referred to as “Control Volume 1”.

Also, Figure 11 depicts the PDFs in a different control volume. This one is a hollow cylinder of inner radius of 1.2 mm, outer radius of 2.5 mm and a height of 6 mm, aligned with the jet cone and also located close to the injection position. Herein, it is referred to as “Control Volume 2”.

Upon comparison of Figures 10 and 11, we observe that droplets at the spray periphery tend to have larger diameters than those located closer to the injection center-line. Additionally, the dispersion of the computed pdfs varies only by a little we switch from Control Volume 1 to Control Volume 2. In other words, the droplet size has the same dispersion close the centerline and at the periphery of the spray. Interestingly, these trends have been predicted by all four breakup models tested herein.

To the best of our knowledge, there are no detailed experimental results for droplet diameter distributions in sprays down to the order of micrometers. This is due to the inherent difficulties of taking measurements for droplets of such small sizes. For this reason, only numerical results of droplet diameter PDFs are presented in figure 9, 10 and 11.

6 Conclusions

In this article we have presented large-eddy simulations of liquid fuel injection, breakup, evaporation and eventual mixing with hot ambient gas. Different droplet breakup models; TAB, RD and PE, were employed and tested. Also, a modified version of the TAB model, referred to as MTAB, is proposed. The performances of these breakup models are assessed by comparing global quantities such as liquid penetration and fuel vapor penetration against the experimental results of SANDIA [10] and IFPEN.

Based on our simulations we conclude that, among the pre-existing models tested herein, the TAB model produces slightly more accurate predictions for the liquid penetration. This is due to the fact that it better encapsulates the underpinning physical mechanisms of droplet breakup. On the other hand, the fuel vapor penetration is overpredicted by all three pre-existing models.

Our numerical tests further indicate that the proposed MTAB model provides mildly improved predictions for both liquid penetration and vapor penetration distances. However, the vapor penetration distance is still slightly overpredicted when compared to the experimental data.

In conclusion, the models examined in our study are based on different physical concepts of droplet disintegration, but none capture all of the relevant modes of the breakup. Consequently discrepancies, in terms of breakup initiation time and duration, exist between the simulations and the experimental results, independent of the model used.

Acknowledgements The first author gratefully acknowledges the financial support of the National Research Fund of Belgium (FNRS) in the form of the ERANET BioCFD program.

References

1. Alderliesten, M.: Mean particle diameters. Part VII. The Rosin-Rammler size distribution: physical and mathematical properties and relationships to moment-ratio defined mean particle diameters. Part. Part. Syst. Char. **30**(3), 244–257 (2013)
2. Amsden, A.A., O'Rourke, P.J., Butler, T.D.: KIVA-II: A computer program for chemically reactive flows with sprays. Los Alamos National Lab. REP. LA-11560-MS DE89012805 (1989)
3. Beatrice, C., Belardini, P., Berteli, C., Camerotti, M., Cirillo, N.C.: Fuel jet models for multidimensional diesel combustion calculation: An update. SAE Int. J. Engines pp. 194–204 (1995)
4. Bianchi, G.M., Pelloni, P.: Modeling the diesel fuel spray breakup by using a hybrid model. In: SAE Technical Paper Series. SAE International (1999)
5. Brodkey, R.S., Addison, W.: The phenomena of fluid motions. J. Fluid Mech. **34**, 821–822 (1968)
6. Burcat, A., Ruscic, B.: Third millenium ideal gas and condensed phase thermochemical database for combustion (with update from active thermochemical tables). Argonne National Laboratory Technical Report ANL-05/20 and Technion – Israel Inst. of Tech. Report TAE 960 (2005)
7. Chai, X., Mahesh, K.: Dynamic k-equation model for large-eddy simulation of compressible flows. J. Fluid Mech. **699**, 385–413 (2012)
8. Dukowicz, J.K.: A particle-fluid numerical model for liquid sprays. J. Comput. Phys. **35**, 229–252 (1980)
9. ECN: Sprays A & B, Engine Combustion Network. <https://ecn.sandia.gov/diesel-spray-combustion/computational-method/modeling-standards/> (2018)
10. ECN: Sprays A & B, Engine Combustion Network. <https://ecn.sandia.gov/diesel-spray-combustion/target-condition/spray-ab/> (2019)
11. Elkotb, M.M.: Fuel atomization for spray modelling. Prog. Energy Combust. Sci. **8**, 61–91 (1982)
12. Faeth, G.M., Hsiang, L.P., Wu, P.K.: Structure and breakup properties of sprays. Int. J. Multiphas. Flow **21**, 99–127 (1995)
13. Favre, A.: Turbulence - space-time statistical properties and behavior in supersonic flows. Phys. Fluids **26**, 2851–2863 (1983)
14. Greifzu, F., Kratzsch, C., Forger, T., Lindner, F., Schwarze, R.: Assessment of particle-tracking models for dispersed particle-laden flows implemented in openfoam and ansys fluent. Eng. Appl. Comput. Fluid Mech. **10**(1), 30–43 (2016)
15. Grosshans, H., Berrocal, E., Kristensson, E., Szász, R.: Prediction and measurement of the local extinction coefficient in sprays for 3D simulation/experiment data comparison. Int. J. Multiphas. Flow **72** (2015)
16. Grosshans, H., Griesing, M., Mönckedieck, M., Hellwig, T., Walther, B., R. Gopireddy, S., Sedelmayer, R., Pauer, W., Moritz, H.U., A. Urbanetz, N., Gutheil, E.: Numerical and experimental study of the drying of bi-component droplets under various drying conditions. Int. J. Heat Mass Transf. **96**, 97–109 (2016)
17. Hsiang, L.P., Faeth, G.M.: Near-limit drop deformation and secondary breakup. Int. J. Multiphas. Flow **18**, 635–652 (1992)
18. Ibrahim, A.E., Yang, H.Q., Przekwas, J.A.: Modeling of spray droplets deformation and breakup. J. Propul. Power **9** (1993)
19. IFPEN: IFPEN experimental data. <https://ecn.sandia.gov/ecn-data-search/> (2019)
20. Issa, R.I.: Solution of the implicitly discretised fluid flow equations by operator-splitting. J. Comput. Phys. **62**(1), 40–65 (1986)
21. Lacaze, G., Misdariis, A., Ruiz, A., Oefelein, J.C.: Analysis of high-pressure Diesel fuel injection processes using LES with real-fluid thermodynamics and transport. Proc. Combust. Inst. **35**(2), 1603 – 1611 (2015)

22. Lamb, H.: *Hydrodynamics*, 6th edn. Dover (1945)
23. Lefebvre, A., McDonell, V.: *Atomization and Sprays*, 2 edn. CRC Press (2017)
24. Liu, A.B., Mather, D., Reitz, R.D.: Modeling the effects of drop drag and breakup on fuel sprays. Technical Paper Series, 930072 (1993)
25. Matheis, J., Hickel, S.: Multi-component vapor-liquid equilibrium model for LES of high-pressure fuel injection and application to ECN spray A. *Int. J. Multiphase Flow* **99**, 294 – 311 (2018)
26. Matysiak, A.: Euler-Lagrange Verfahren zur Simulation tropfenbeladener Strömung in einem Verdichtergitter. Ph.D. thesis, Helmut-Schmidt Universität, Hamburg (2007)
27. Moin, P., Squires, K., Cabot, W., Lee, S.: A dynamic subgrid-scale model for compressible turbulence and scalar transport. *Phys. Fluids A: Fluid Dyn.* **3**(11), 2746–2757 (1991)
28. Nicholls, J.A.: Stream and droplet breakup by shock waves. NASA-SP-194 Technical Report pp. 126–128 (1972)
29. Nicholson, L., Fang, X., Camm, J., Davy, M., Richardson, D.: Comparison of transient diesel spray break-up between two computational fluid dynamics codes. SAE International (2018)
30. O'Rourke, P.J., Amsden, A.A.: The TAB method for numerical calculation of spray droplet breakup. In: SAE Technical Paper Series, 872089. SAE International (1987)
31. Park, J.H., Yoon, Y., Hwang, S.S.: Improved tab model for prediction of spray droplet deformation and breakup. *Atomization Spray* **12**(4), 387–401 (2002)
32. Pickett, L.M., Abraham, J.P.: Computed and measured fuel vapor distribution in a diesel spray. *Atomization Spray* **20**(3), 241 – 250 (2010)
33. Pilch, M.: Acceleration induced fragmentation of liquid drops. Ph.D. thesis, Univ. of Virginia (1981)
34. Pilch, M., Erdman, C.A.: Use of breakup time data and velocity history data to predict the maximum size of stable fragments for acceleration-induced breakup of a liquid drop. *Int. J. Multiphas. Flow* **13**, 741–757 (1987)
35. Ranz, W.E., Marshall, W.R.: Evaporation from drops: Part I. *Chem. Engr. Prog.* **48**(3), 141–146 (1952)
36. Ranz, W.E., Marshall, W.R.: Evaporation from drops: Part II. *Chem. Engr. Prog.* **48**(3), 173–180 (1952)
37. Reinhardt, Y., Kleiser, L.: Validation of particle-laden turbulent flow simulations including turbulence modulation. *J. Fluids Eng.* **137**(7) (2015)
38. Reitz, R., Bracco, V.F.: Mechanisms of breakup of round liquid jets. In: *Encyclopedia of Fluid Mechanics*, vol. 3, pp. 233–249 (1986)
39. Reitz, R.D., Diwakar, R.: Structure of high-pressure fuel sprays. In: SAE Technical Paper Series, 870598. SAE International (1987)
40. Sirignano, W.A.: *Fluid Dynamics and Transport of Droplets and Sprays*, 2 edn. Cambridge University Press (2010)
41. Solsvik, J., Skjervold, V.T., Han, L., Luo, H., Jakobsen, H.A.: A theoretical study on drop breakup modeling in turbulent flows: The inertial subrange versus the entire spectrum of isotropic turbulence. *Chem. Eng. Sci.* **149**, 249 – 265 (2016)
42. Tanner, F.X.: Liquid jet atomization and droplet breakup modeling of non-evaporating diesel fuel sprays. In: SAE Technical Paper Series, 970050. SAE International (1997)
43. Vesilind, P.A.: The rosin-rammler particle size distribution. *Resour. Recovery Conserv.* **5**, 275–277 (1980)
44. Weller, H.G., Tabor, G., Jasak, H., Fureby, C.: A tensorial approach to computational continuum mechanics using object-oriented techniques. *Comput. Phys.* **12**, 620–631 (1998)
45. Wierzba, A.: Deformation and breakup of liquid drops in a gas stream at nearly critical weber numbers. *Exp. Fluids* **9**(1), 59–64 (1990)
46. Wu, P.K., Faeth, G.M.: Aerodynamic effects on primary breakup of turbulent liquids. *Atomization Spray* **3**, 265–289 (1993)
47. Yang, S., Yi, P., Habchi, C.: Real-fluid injection modeling and LES simulation of the ECN spray A injector using a fully compressible two-phase flow approach. *Int. J. Multiphase Flow* **122**, 103–145 (2020)

-
48. Yoon, S.S., Hewson, J., DesJardin, P.E., Glaze, D., Black, A.R., Skaggs, R.R.: Numerical modeling and experimental measurements of a high speed solid-cone water spray for use in fire suppression applications. *Int. J. Multiphas. Flow* **30**, 1369–1388 (2004)
 49. Yoshizawa, A.: Statistical theory for compressible turbulent shear flows, with the application to subgrid modeling. *Phys. Fluids* **29**, 2152–2164 (1987)